Quantum State Engineering of a Hubbard System with Ultracold Fermions

Christie S. Chiu, Geoffrey Ji, Anton Mazurenko, Daniel Greif, and Markus Greiner

Quantum state engineering of a Hubbard system with ultracold fermions

Christie S. Chiu, Geoffrey Ji, Anton Mazurenko, Daniel Greif, and Markus Greiner*

Department of Physics, Harvard University, Cambridge, Massachusetts, 02138, USA

(Dated: May 15, 2018)

Accessing new regimes in quantum simulation requires development of new techniques for quantum state preparation. We demonstrate quantum state engineering of a strongly-correlated many-body state of the two-component repulsive Fermi-Hubbard model on a square lattice. Our scheme makes use of an ultra-low entropy doublon band insulator created through entropy redistribution. After isolating the band insulator, we change the underlying potential to expand it into a half-filled system. The final many-body state realized shows strong antiferromagnetic correlations and a temperature below the exchange energy. We observe an increase in entropy, which we find is likely caused by the many-body physics in the last step of the scheme. This technique is promising for low-temperature studies of cold-atom-based lattice models.

Understanding and controlling complex many-body quantum physics is an important research frontier in quantum information, condensed matter physics, and quantum chemistry. Quantum simulation has emerged as a powerful tool for computing many-body quantum phases and dynamics, with the potential to exceed simulations on classical computers [1, 2]. By engineering highly coherent many-body systems, a wide variety of Hamiltonians can be studied [3]. A unique platform for scalable quantum simulation is ultracold atoms, where the development of quantum gas microscopy has enabled control at the single atom level [4, 5]. Quantum simulation extends to other promising platforms such as ion traps, superconducting circuits, solid state systems, Rydberg atoms, and photonic systems [6–11].

A major challenge of all these platforms is creating a coherent quantum many-body state, which is often the ground state. Traditionally, cold atom experiments in optical lattices realize quantum states by loading an evaporatively cooled quantum gas into the lattice potential [12]. This approach has been very successful [13–15], but the minimum achievable temperatures for fermionic systems are limited by reduced cooling efficiency at low temperatures. An alternative approach is quantum state engineering. Generally, this method realizes an isolated pure quantum state by initializing one wavefunction under an initial Hamiltonian, then changing the Hamiltonian while preserving coherence during time evolution so that the accompanying wavefunction becomes the target state (see Fig. 1). Several platforms have used different versions of quantum state engineering to create desired quantum states [16–20], and schemes have been proposed for ultracold fermionic atoms [21–23]. The site-resolved readout and control afforded by quantum gas microscope experiments [4, 5, 24–31] are perfect tools to implement quantum state engineering of many-body states of ultracold fermionic atoms in optical lattices.

Here we demonstrate quantum state engineering for a many-body state of fermionic atoms in the Hubbard
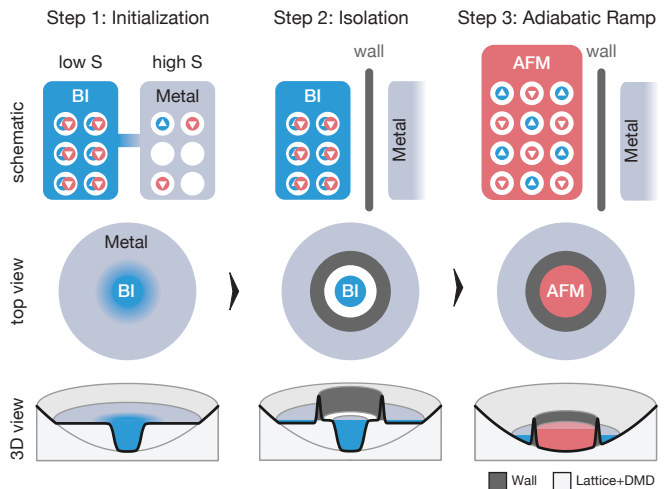

FIG. 1. (color online). Illustration of the quantum state engineering scheme. (Top row) A low-density metallic state removes entropy from a band insulator (BI), after which the two states can be isolated thermally. The BI can then be ramped into an antiferromagnetic (AFM) state by increasing the number of available sites. (Middle row) Map of density inhomogeneity and states in our experimental setup. (Bottom row) We implement our scheme by engineering optical potential landscapes to change the Hamiltonian at each step (see main text and [32]).

model. This model describes spin-$1/2$ fermions on a lattice with nearest-neighbor tunneling t and repulsive on-site interaction U. Under this model, a coexistence of phases can be realized through inhomogenous particle density in global thermal equilibrium [34]. A metal exists at low particle density, characterized by a large density of states and high entropy per particle. At half-filling (one particle per site), an antiferromagnet emerges, where spins arrange in an alternating pattern. This phase is gapped in the charge sector by U, but has nonzero density of states due to low-energy spin excitations. The band insulator (BI) appears when the band is completely

filled with two particles per site, and thus has a large energy gap equal to the bandgap, vanishing density of states, and vanishing entropy per particle. Because of the differing density of states, under fixed global atom number and global entropy the density inhomogeneity can be engineered to produce low-entropy states.

If a BI and metal are in thermal contact, entropy flows from the BI into the metal, see Fig. 1. By using a fully gapped state, we optimize this entropy redistribution technique [13, 21, 22, 26]. The result is an ultra-low entropy BI initial state with an entropy per particle as low as $0.016(3) k_B$ in units of the Boltzmann constant, over an order of magnitude lower than the lowest value previously achieved with entropy redistribution [26]. In the next step we thermally isolate the low-entropy region by suppressing particle transport between the BI and reservoir. Finally, we convert the gapped BI into a strongly-correlated many-body state at half-filling. This final state has a nearest-neighbor spin correlator of $C_1 = -0.21(1)$ reflecting strong antiferromagnetic character and a temperature of $k_B T/t = 0.46(2)$.

Our experimental setup consists of a balanced spin mixture of the two lowest hyperfine states of fermionic ^{6}Li in a combined square optical lattice and blue-detuned potential. We set $t/h = 0.89(1)$ kHz in units of the Planck constant and $U/t = 7.7(3)$ or $U/t = 5.9(2)$ [32]. The quantum gas lies in the object plane of a quantum gas microscope [32], allowing both atom imaging and potential control at the site-resolved level [33]. Such precise control is achieved by placing two digital micromirror devices (DMD1 and DMD2) in the image plane and projecting their patterns with blue-detuned light [32]. The DMD1 pattern is designed to engineer the coexistence of phases through changing the optical potential and therefore particle density across the sample, as in [26]. DMD2 creates the isolating wall in the second step of our scheme.

The success of quantum state engineering schemes fundamentally depends upon initial state preparation. The initial density distribution consists of two regions of constant but different density: the doublon-filled center and the surrounding metallic reservoir (see Fig. 2a), created with DMD1 by setting the potential offset between the two regions to $\Delta \approx 2U$. Following entropy redistribution we achieve an ultra-low entropy BI of more than 130 sites. Due to light-assisted collisions which occur during the imaging process, sites initially containing doublons appear as empty [33]. We obtain the entropy per particle on a single site from the measured singles density n_s [32]. The average singles density $\overline{n}_s$ across the BI region is $0.4(1)\%$, corresponding to an upper bound for the average entropy per particle across the region of $0.016(3) k_B$. This signifies a 50-fold reduction in entropy compared to a homogenous system, showing that the technique is highly efficient [32]. This entropy is significantly lower than that of the lowest-entropy two-component BIs realized in cold-atom systems thus far [25, 34].
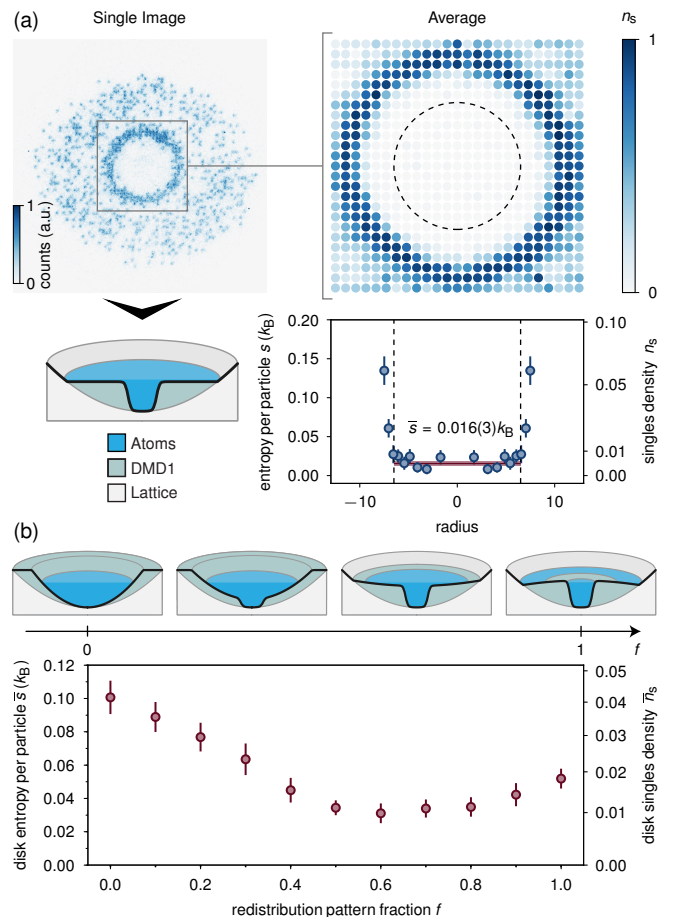

FIG. 2. (color online). Ultra-low entropy BI at $U/t = 7.7(3)$. (a) Raw fluorescence image of single BI, optical potential schematic, and average density map of 50 BI realizations. Through entropy redistribution, we create a BI with > 130 sites and average entropy per particle $0.016(3) k_B$. Error bars denote standard error of 50 measurements and azimuthal averaging. (b) By continuously tuning the optical potential between a harmonic trap and our entropy redistribution pattern at constant BI size at $U/t = 5.9(2)$, we see a decrease in BI entropy due to increased entropy redistribution efficiency. The final pattern yields a slightly higher entropy than the optimum, but is necessary for our scheme. Error bars denote standard error of >20 measurements each with 133 lattice sites.

Most cold atom experiments take place in a harmonic trap, where some entropy redistribution is already present because of inhomogenous particle density. We compare entropy redistribution efficiencies between a harmonic pattern and the employed pattern for quantum state engineering by interpolating linearly between these two profiles, parameterized by the fraction f. Atom number, total entropy, and BI size are kept constant. As shown in Fig. 2b, entropy redistribution reduces the BI entropy per particle by more than a factor of 3 compared to the harmonic trap, even for a pattern which has not been optimized for redistribution efficiency as in Fig. 2a.

We find a slight increase in entropy moving to the final pattern, which may result from a denser reservoir or from a loss of thermal contact between the system and reservoir. Indeed, the $f = 1$ pattern exhibits a ring of zero density between these two regions. This ring is necessary in the next step of the quantum state engineering scheme.

After initializing the low-entropy BI, the next step is to isolate it from the remaining atoms. We adjust the entropy redistribution pattern such that the BI is surrounded by holes, see Fig. 3a. To ensure full isolation of the BI, we subsequently raise a circular wall with a thickness of about 3 sites using DMD2 [32]. We set the wall diameter to a value larger than the BI size. The region Ω inside the wall therefore contains both the BI and empty sites. For the shape of the BI we choose either a circular 12-site diameter disk (similar to the $f = 1$ configuration) or a rectangular 8-site by 12-site box. Both regions in Ω are approximately homogenous in density with energy
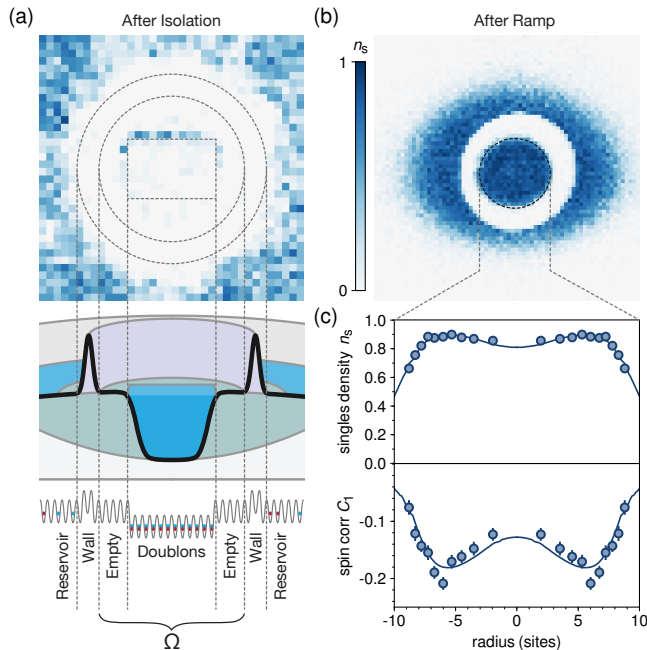

FIG. 3. (color online). (a) Average density map (40 realizations) and configuration of entropy redistribution at $U/t = 5.9(2)$ after isolation. Imperfections in the optical potential manifest as singly-occupied sites, as seen at the upper edge of the box. (b) Average density map of 41 images after ramp highlighting how the insulating wall separates the inner and outer regions, with initialization via disk pattern. (c) Corresponding density and nearest-neighbor correlator profiles vs. radius after ramp. The nearest-neighbor correlations are antiferromagnetic with a strength of up to $C_1 = -0.21(1)$. A simultaneous fit to both profiles (solid line) gives a temperature of $k_B T/t = 0.46(2)$. The fit is limited to radius 9, to avoid effects from the insulating wall. Error bars denote standard error of >40 sets of correlation maps and azimuthal averaging. For (b)+(c), $U/t = 7.7(3)$.

offset $\Delta \approx 2U$. To ensure the two regions have the desired densities, we set the global chemical potential inside Ω to a value below Δ by adjusting the total atom number [32].

For the box-shaped configuration (see Fig. 3a), the entropy per particle within Ω is $0.25(1)\,k_B$. This entropy is greater than that of the pure BI because it includes both doublon and hole regions; indeed, the pure BI entropy per particle away from the box edge is only $0.08(1)\,k_B$, so the greatest entropy contribution to Ω is from the boundary between the regions. More specifically, if the box potential is not perfectly aligned with the lattice sites, the potential offset on sites close to the edge can be modified. Even if the box is aligned, the microscope point spread function smooths the potential across one or two lattice sites. These effects lead to density defects on both sides of the box edge that are visible as singly-occupied sites and increased entropy, see for example the upper box edge in Fig. 3a. The ring-shaped wall has a negligible effect on initial entropy, confirmed through comparing the entropy with and without the wall.

The final step in our quantum state engineering scheme is to convert the initial state into the target many-body state. For this measurement we use the disk pattern for the BI to reduce alignment sensitivity. To ensure half-filling in the final state, the wall diameter is set such that the number of holes and doublons within Ω is approximately equal. After initialization and isolation we slowly remove the potential offset between holes and doublons by reducing the DMD1 laser power [32]. In Fig. 3b we show the measured singles density n_s after a $40\,\text{ms}$ linear ramp of the potential offset. The atomic density extends over the entire region Ω and sharply decreases at the inner edge of the wall, indicating particle transport has occurred from the doublon core to the surrounding empty sites. The inner and outer regions are separated by the insulating wall, marked by a ring of empty sites. In the final state, atoms in Ω are expected to show antiferromagnetic correlations, whose strength reflect the adiabaticity of the ramp. The nearest-neighbor spin correlations, measured with a technique established in previous work [35], are strongly antiferromagnetic with values up to $C_1 = 4\langle \hat{S}_i^z \hat{S}_{i+1}^z \rangle = -0.21(1)$. Here $\hat{S}_i^z$ denotes the standard spin-1/2 operator along the z-direction on site i. These observations demonstrate a successful implementation of quantum state engineering, where a strongly-correlated many-body state is created from an initially uncorrelated BI of doublons.

Locally changing density and spin correlations within Ω originate from the underlying harmonic confinement created by the lattice lasers. The maximum in the singles density radial profile indicates the density is above half-filling in the center and continuously decreases for larger radii, see Fig. 3c. We intentionally keep this confinement to study whether the system is in thermal equilibrium. When applying a simultaneous fit of exact theoretical

predictions to both measured radial profiles with shared fit parameters, we find reasonable agreement [35, 36]. This shows that the system within Ω is consistent with a thermal equilibrium state. In order to determine whether deviations from thermal equilibrium or finite-size effects are present, more detailed knowledge of corrections to the exact confinement potential is required.

From the fit we obtain a temperature in Ω of $k_\mathrm{B}T/t = 0.46(2)$, which is comparable to the temperatures achieved so far in harmonic traps [31], but still higher than the lowest value of $k_\mathrm{B}T/t = 0.25(2)$ achieved with entropy redistribution [26]. Although this temperature is surprisingly low given the simple ramp scheme used here, the system is still far from the ground state. Besides the nonzero entropy of the initial BI, this nonzero temperature may result from non-adiabaticity of the ramp or residual heating. We now explore both possibilities.

We first study non-adiabaticity by examining the entropy increase after completing and reversing the offset ramp [32]. For this measurement we use the box pattern for the lowest initial entropy in Ω. As heating effects are negligible in the initial state, a perfectly adiabatic process implies measuring the same entropy as this initial state. When varying the endpoint of the ramp Δ_f, we find that the entropy per particle increases steadily as the ramp endpoint decreases, see Fig. 4a. The qualitative shape of the curve suggests a lack of adiabaticity largely throughout the second half of the ramp. In this regime, $\Delta \approx U$ and particles can freely tunnel out of the doublon core. For the full two-way ramp, we find an entropy increase of $0.46(2)\,k_\mathrm{B}$. Although this increase strongly indicates a non-adiabatic ramp, it may actually be caused by greater heating rates during the ramp, for example due to changes in the many-body energy spectrum.

To distinguish heating during the ramp from non-adiabaticity, we measure the heating rate for each ramp endpoint by holding for a variable time τ_h before reversing the ramp and measuring the resulting entropy [32]. Heating rates are generally greater than the initial heating rate, with values up to $2.1(2)\,k_\mathrm{B}/\mathrm{s}$, see Fig. 4b. The observed increase in heating rate at $\Delta \approx U$ indicates a drastic change in the many-body energy spectrum, as already suggested by the non-adiabaticity measurement of Fig. 4a. From the measured rates, we estimate an entropy increase from heating of $0.06\,k_\mathrm{B}$ for the full ramp. This indicates that the majority of entropy increase does not originate from heating, but rather from non-adiabaticity. When decreasing the ramp rate for the full two-way ramp, the final entropy increases, indicating that any improvement in adiabaticity is insufficient to overcome heating during the additional ramp time.

Despite the non-adiabaticity, achievement of low temperatures with such a simple ramp scheme is encouraging. A possible improvement is to reduce the amount of required particle transport, which may reduce the non-

adiabaticity. We repeat the adiabaticity measurement for an initial system consisting of alternating stripes of holes and doublons surrounded by a box-shaped wall, see bottom right panel of Fig. 4a. While the initial entropy is worse than that of the box due to the more complex potential landscape, crucially this configuration yields no significant improvement in entropy increase. This
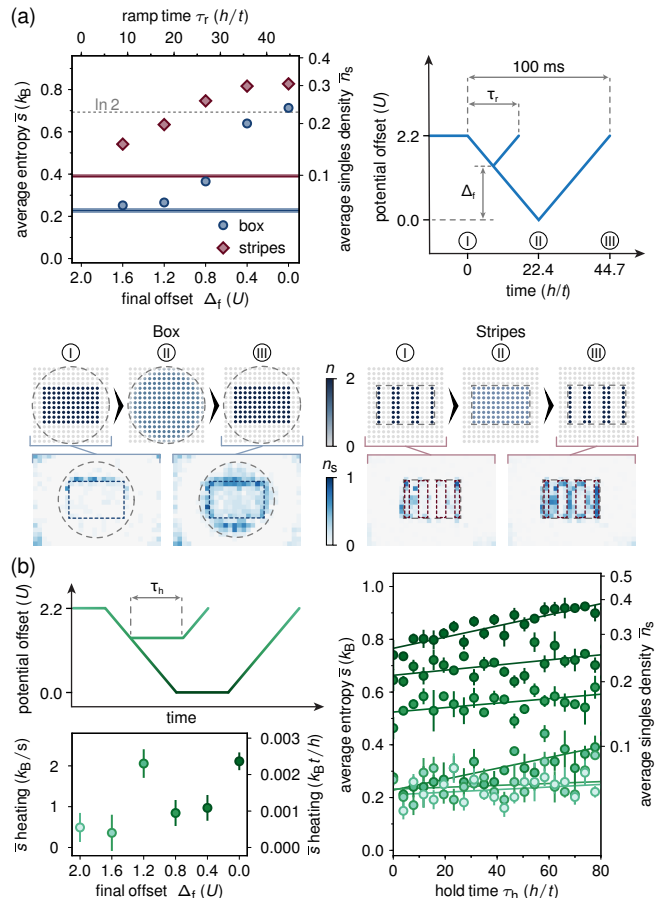

FIG. 4. (color online). Examining final ramp adiabaticity at $U/t = 5.9(3)$. (a) A round trip measurement beginning with an isolated box of doublons surrounded by holes demonstrates non-adiabaticity predominantly in the second half of the offset ramp-off (circles). Adiabaticity is not significantly improved by initializing the holes and doublons in stripes (diamonds). Horizontal lines with shading indicate reference measurements and uncertainty, taken with no ramp. Lower panels show schematic images for the particle density n and measured average singles density maps for the box (left) and stripe (right) configurations at different times throughout the round-trip ramp. Dashed lines indicate the wall inner edge, while dotted lines enclose BI regions. Error bars are smaller than the markers, and denote standard error of 40 (187) measurements for the box (stripe) pattern. (b) We quantify heating rates at various points throughout the ramp (upper left), which enable us to approximate the contribution of entropy increase due to heating. Error bars for entropy measurements (right) denote standard error of 5 measurements; error bars for heating rates (lower left) are from the fits.

suggests that the dominant reason for non-adiabaticity lies within the many-body physics occurring during the ramp, which strongly depends on how the ramp is implemented and what intermediate phases are crossed [37–39]. An improvement could be to avoid a closing charge gap in the many-body spectrum during the ramp, possibly by using a double-well superlattice. Such a configuration has been predicted to be very efficient in numerical simulations [23, 40].

In conclusion, we have implemented a quantum state engineering scheme to create a fermionic many-body state. Through adjusting the initial balance of doubly-occupied and unoccupied sites, this technique offers the flexibility to vary the doping of the sample on the single-atom level. Furthermore, the remarkably low initial entropies afforded by entropy redistribution may enable even lower temperatures at arbitrary doping to search for signatures of a d-wave superfluid state [41]. However, additional studies must be conducted to determine the optimum path in parameter space which minimizes the entropy. Analogous quantum state engineering schemes can be designed for studies of stripe phases with strongly magnetic atoms, massively entangled spin states, and adiabatic quantum computation [42–44].

---

* greiner@physics.harvard.edu

[1] R. P. Feynman, International Journal of Theoretical Physics **21**, 467 (1982).

[2] S. Lloyd, Science **273**, 1073 (1996).

[3] I. M. Georgescu, S. Ashhab, and F. Nori, Reviews of Modern Physics **86**, 153 (2014).

[4] W. S. Bakr, A. Peng, M. E. Tai, R. Ma, J. Simon, J. I. Gillen, S. Foelling, L. Pollet, and M. Greiner, Science **329**, 547 (2010).

[5] J. F. Sherson, C. Weitenberg, M. Endres, M. Cheneau, I. Bloch, and S. Kuhr, Nature **467**, 68 (2010).

[6] I. Bloch, J. Dalibard, and S. Nascimbène, Nature Physics **8**, 267 (2012).

[7] R. Blatt and C. F. Roos, Nature Physics **8**, 277 (2012).

[8] A. Aspuru-Guzik and P. Walther, Nature Physics **8**, 285 (2012).

[9] H. Weimer, M. Müller, I. Lesanovsky, P. Zoller, and H. P. Büchler, Nature Physics **6**, 382 (2010).

[10] M. H. Devoret and R. J. Schoelkopf, Science **339**, 1169 (2013).

[11] D. D. Awschalom, L. C. Bassett, A. S. Dzurak, E. L. Hu, and J. R. Petta, Science **339**, 1174 (2013).

[12] I. Bloch, J. Dalibard, and W. Zwerger, Reviews of Modern Physics **80**, 885 (2008).

[13] T. Esslinger, Annual Reviews of Condensed Matter Physics **1**, 129 (2010).

[14] D. Greif, T. Uehlinger, G. Jotzu, L. Tarruell, and T. Esslinger, Science **340**, 1307 (2013).

[15] R. A. Hart, P. M. Duarte, T.-L. Yang, X. Liu, T. Paiva, E. Khatami, R. T. Scalettar, N. Trivedi, D. A. Huse, and R. G. Hulet, Nature **519**, 211 (2015).

[16] C. Roos, T. Zeiger, H. Rohde, H. C. Nägerl, J. Eschner, D. Leibfried, F. Schmidt-Kaler, and R. Blatt, Physical Review Letters **83**, 4713 (1999).

[17] R. Islam, E. Edwards, K. Kim, S. Korenblit, C. Noh, H. Carmichael, G.-D. Lin, L.-M. Duan, C.-C. Joseph Wang, J. Freericks, and C. Monroe, Nature Communications **2**, 377 (2011).

[18] J. Simon, W. S. Bakr, R. Ma, M. E. Tai, P. M. Preiss, and M. Greiner, Nature **472**, 307 (2011).

[19] H. Labuhn, S. Ravets, D. Barredo, L. Béguin, F. Nogrette, T. Lahaye, and A. Browaeys, Physical Review A **90**, 023415 (2014).

[20] H. Bernien, S. Schwartz, A. Keesling, H. Levine, A. Omran, H. Pichler, S. Choi, A. S. Zibrov, M. Endres, M. Greiner, V. Vuletić, and M. D. Lukin, Nature **551**, 579 (2017).

[21] J.-S. Bernier, C. Kollath, A. Georges, L. De Leo, F. Gerbier, C. Salomon, and M. Köhl, Physical Review A **79**, 061601(R) (2009).

[22] T.-L. Ho and Q. Zhou, arXiv:0911.5506v1.

[23] M. Lubasch, V. Murg, U. Schneider, J. I. Cirac, and M.-C. C. Bañuls, Physical Review Letters **107**, 165301 (2011).

[24] E. Haller, J. Hudson, A. Kelly, D. A. Cotta, B. Peaudecerf, G. D. Bruce, and S. Kuhr, Nature Physics **11**, 738 (2015).

[25] L. W. Cheuk, M. A. Nichols, K. R. Lawrence, M. Okan, H. Zhang, E. Khatami, N. Trivedi, T. Paiva, M. Rigol, and M. W. Zwierlein, Science **353**, 1260 (2016).

[26] A. Mazurenko, C. S. Chiu, G. Ji, M. F. Parsons, M. Kanász-Nagy, R. Schmidt, F. Grusdt, E. Demler, D. Greif, and M. Greiner, Nature **545**, 462 (2017).

[27] T. A. Hilker, G. Salomon, F. Grusdt, A. Omran, M. Boll, E. Demler, I. Bloch, and C. Gross, Science **357**, 484 (2017).

[28] G. J. A. Edge, R. Anderson, D. Jervis, D. C. McKay, R. Day, S. Trotzky, and J. H. Thywissen, Physical Review A **92**, 063406 (2015).

[29] M. Miranda, R. Inoue, Y. Okuyama, A. Nakamoto, and M. Kozuma, Physical Review A **91**, 063414 (2015).

[30] R. Yamamoto, J. Kobayashi, T. Kuno, K. Kato, and Y. Takahashi, New Journal of Physics **18**, 023016 (2016).

[31] P. T. Brown, D. Mitra, E. Guardado-Sanchez, P. Schauß, S. S. Kondov, E. Khatami, T. Paiva, N. Trivedi, D. A. Huse, and W. S. Bakr, Science **357**, 1385 (2017).

[32] See Supplemental Material [url], which includes Refs. [26], [35-36], [45].

[33] M. F. Parsons, F. Huber, A. Mazurenko, C. S. Chiu, W. Setiawan, K. Wooley-Brown, S. Blatt, and M. Greiner, Physical Review Letters **114**, 213002 (2015).

[34] D. Greif, M. F. Parsons, A. Mazurenko, C. S. Chiu, S. Blatt, F. Huber, G. Ji, and M. Greiner, Science **351**, 953 (2016).

[35] M. F. Parsons, A. Mazurenko, C. S. Chiu, G. Ji, D. Greif, and M. Greiner, Science **323**, 1253 (2016).

[36] E. Khatami and M. Rigol, Physical Review A **84**, 053611

(2011).

[37] A. Fubini, G. Falci, and A. Osterloh, New Journal of Physics **9**, 134 (2007).

[38] L. Cincio, J. Dziarmaga, J. Meisner, and M. M. Rams, Physical Review B **79**, 094421 (2009).

[39] T. M. Hoang, H. M. Bharath, M. J. Boguslawski, M. Anquez, B. A. Robbins, and M. S. Chapman, PNAS **113**, 9475 (2016).

[40] A. Kantian, S. Langer, and A. J. Daley, arXiv:1609.03579v1.

[41] P. A. Lee, N. Nagaosa, and X. G. Wen, Reviews of Modern Physics **78**, 17 (2006).

[42] A. Mazloom, B. Vermersch, M. A. Baranov, and M. Dalmonte, Physical Review A **96**, 033602 (2017).

[43] Z. Zhang and L.-M. Duan, Physical Review Letters **111**, 180401 (2013).

[44] E. Farhi, J. Goldstone, S. Gutmann, J. Lapan, A. Lundgren, and D. Preda, Science **292**, 472 (2001).

[45] G. Zürn, T. Lompe, A. N. Wenz, S. Jochim, P. S. Julienne, and J. M. Hutson, Physical Review Letters **110**, 135301 (2013).